Experimental Mechanics (2019) 59:337–347
https://doi.org/10.1007/s11340-018-00451-6

In-Situ Nanoindentation Measurement of Local Mechanical Behavior of a Li-Ion Battery Cathode in Liquid Electrolyte

L.S. de Vasconcelos[1] · N. Sharma[1] · R. Xu[1] · K. Zhao[1]

Received: 3 June 2018 / Accepted: 29 October 2018 / Published online: 28 November 2018

Abstract

The state-of-the-art cathode materials experience severe structural and mechanical degradation over lithiation cycles albeit their small deformation. It has been a great challenge to characterize the mechanical behavior of composite electrodes in-situ and in real-time because of their environmental sensitivity and intricate microscopic heterogeneity. We use nanoindentation to measure the in-situ mechanical behavior of individual phases in a cathode composite electrode $LiNi_xMn_yCo_zO_2$. We focus on the understanding of the mechanical properties of the constituents in dry and wet conditions. We evaluate the influence of electrolyte soaking on the elastic modulus, hardness, and volume change of the conductive matrix with different degrees of porosity. More interestingly, we measure the modulus, hardness, and fracture strength of agglomerated active particles and sintered pellets, and compare their mechanical properties in the dry and liquid environment. We show that the electrolyte enhances the fracture strength of NMC agglomerated particles. The increase in interfacial strength may be a result of the additional capillary force between primary particles. Results offer mechanistic understanding of the complex behavior of composite electrodes and will feed chemomechanical models on Li-ion batteries.

Keywords Nanoindentation · *In situ* · NMC · Mechanical properties · Li-ion batteries

Introduction

Mechanical degradation is currently a major challenge in the development of high energy density Li-ion batteries and solid-state batteries [1–3]. The repetitive deformation during Li insertion and extraction creates long-range stresses within the active materials, solid electrolyte interface (SEI), and along the interfaces between electrodes and the Li/electron conductive agents. Mechanical stresses induce material defects such as dislocations [4, 5], cavities [6], and cracks [7–9] throughout the active material, rupture of the SEI layer, and separation of electrodes from the conductive network [10, 11]. The constant disruption of the solid interfaces leads to Li depletion, increase of ohmic and thermal resistances, and steady fade of cyclic efficiency, while the isolation of the active materials results in a mostly immediate loss in capacity of batteries [12, 13].

Mechanical issues are an overwhelming problem in electrodes of intrinsically large volumetric expansion such as conversion- and insertion-type anodes [14–18]. Limited success has been achieved to mitigate their mechanical failure upon Li reactions. For cathode materials that undergo a much less obvious volumetric strain (~5%), structural degradation is less recognized. In recent years, experiments have shown that the state-of-the-art cathode materials such as lithium nickel manganese cobalt oxides (NMC) experience significant intergranular and intragranular failure [19, 20]. Intragranular failure normally takes place in abusive operating conditions such as high temperature and high voltage, where oxygen release and extra Li insertion amplify the internal strain within the grain. Intergranular fracture is the cause of structural disintegration of NMC secondary particles. As-synthesized NMC materials are often in the form of "meatball' secondary particles composed of an agglomerate of smaller and anisotropic primary particles. This hierarchical structure is vulnerable to intergranular fracture because the weakly bonded interface cannot sustain internal stresses developed from the anisotropic expansion of the primary particles [21, 22]. The structural

Electronic supplementary material The online version of this article (https://doi.org/10.1007/s11340-018-00451-6) contains supplementary material, which is available to authorized users.

✉ K. Zhao
kjzhao@purdue.edu

[1] School of Mechanical Engineering, Purdue University, West Lafayette, IN 47907, USA

decohesion clearly contributes to the increase of impedance of NMC cathodes over cycles [23, 24].

The mechanical behavior of the inactive materials also plays a role in the electrochemical performance of electrodes. For instance, stiff binders can help contain excessive deformation of active materials during (de)lithiation, maintaining better contact with the conductive matrix and preventing pulverized active particles from disintegrating [25, 26]. At the same time, however, mechanical confinement promotes higher mechanical stresses within the active materials, lowering the accessible capacity [27, 28]. In addition, stiffer binders can lead to severe cracking of the conductive matrix and promote interface fracture depending on the binder/particle contact geometry [29, 30].

The knowledge about the mechanical behavior of electrodes is crucial in understanding the degradation mechanism and in the design of materials of enhanced mechanical reliability. Ex-situ nanoindentation has been widely used in the characterization of electrode materials, owing to its high spatial resolution and ability to access a range of material behaviors [31–33]. More interestingly, many studies probed the evolution of mechanical properties with lithium concentration and in the course of electrochemical cycles [34–38]. However, mechanical characterization of composite electrodes in-situ and in real-time has been a great challenge. The mechanical properties evolve with the state of charge and the cycle number. Furthermore, the operation of batteries is highly sensitive to air – a trace of oxygen and moisture can cause numerous side reactions [39]. The mechanical measurements performed ex-situ and without environmental control may substantially deviate from the electrochemical conditions in real batteries. A few recent noteworthy papers reported the effect of the liquid environment. Wang et al. [40] found that the mechanical response of Si electrodes is dominated by the polyvinylidene fluoride (PVDF) binder and is highly sensitive to the electrolyte solution. Wendt et al. [41] observed that even the customary washing of electrodes using dimethyl carbonate (DMC) solvent can significantly affect measurements because of the large amount of solvent absorbed by the PVDF binder. The studies on the macroscopic behavior of electrodes in liquid electrolyte are valuable. Nevertheless, we would like to point out that electrodes in commercial batteries are highly heterogeneous. First, the mechanical properties of the active particles, polymeric binders, and porous conductive matrix are vastly different. And second, the stress field, Li concentration, and mechanical failure are strongly dependent on the local details of the microstructure of electrodes. The averaged and overall response of composite electrodes is insufficient to unravel their intricate microstructural features and to understand the evolving nature of material states and stress field upon Li reactions.

We recently built an experimental platform of operando nanoindentation to map the local mechanical behavior of electrodes in a liquid cell and in an argon-filled environment [42]. Here we use nanoindentation to measure the in-situ mechanical behavior of individual phases in a commercial $LiNi_{0.5}Mn_{0.3}Co_{0.2}O_2$ (NMC532) electrode which is the current choice of cathode for electric vehicles. We focus on the understanding of the mechanical properties of the constituents in dry and wet conditions, Fig. 1. We compare the influence of the electrolyte solution on NMC particles as well as sintered NMC pellets. For the first time, we show that the electrolyte plays an important role in the fracture strength of NMC secondary particles. The increase in interfacial strength may be a result of the additional capillary force between primary particles. Furthermore, we perform experiments to investigate the influence of electrolyte soaking on the elastic modulus, hardness, and volume change of the conductive matrix with different degrees of porosity. Results offer mechanistic understanding of the complex behavior in composite electrodes and will feed the parametric input of chemomechanical models.

Experimental Methods

Preparation of NMC Samples NMC is prepared in two forms: as-received hierarchical particles (small grains) and sintered pellet (large grains). Commercial NMC532 powder (MTI Co.) is used in the preparation of both configurations. To allow indentation testing, a rigid matrix is necessary to hold the NMC particles in place. The matrix must remain mechanically stable in dry versus wet conditions to avoid changes in the mechanical properties of the matrix from being misinterpreted as changes of the particles. The PVDF binder used in commercial batteries is known to soften in the electrolyte [43] and thus it is not suitable as the matrix for indentation tests on wet NMC. Hence, the inert polystyrene (PS) plastic is selected in our experiments. We perform indentation tests on the PS in

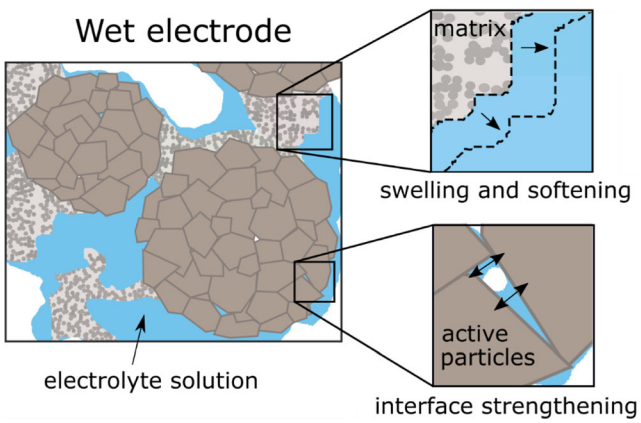

Fig. 1 Sketch of the mechanical behavior of a composite electrode in the liquid electrolyte. Compared to the dry state, the polymeric matrix swells in the volume and softens in the mechanical properties, while the liquid bridging at the interface of the primary particles enhances the interfacial strength

dry and wet environments to confirm its stability in the electrolyte solution. In the sample preparation, the PS granules are first heated to roughly 245 °C on a heat plate. Next, the as-received NMC 532 powder is lightly pressed onto the PS surface with a glass slide and subsequently left to cool down at ambient temperature. For the NMC pellet, as-received NMC 532 powder is first ball milled into submicron primary particles. The stainless-steel container and milling balls are solely used for NMC powder and are cleaned with acetone and isopropyl alcohol before use. Then, approximately 1g of the milled powder is pressed into a die (13 mm) under an applied compressive load of 5 tons (model 4350, Carvar). The compressed pellet is sintered at 1000 °C for 10 h with a heating rate of 10°C/min and left in the furnace until cooled. X-ray diffraction (XRD, Panalytical Empyrean Powder X-ray diffractometer) is performed using a diffractometer with Cu K-alpha radiation in a 2θ range of 10–80° at 40 mA and 45 kV. Both configurations, NMC particle in the PS matrix and sintered NMC pellet, are polished for roughly 30 min using 0.05 μm colloidal silica slurry on imperial cloth (LECO Co.) and dried overnight in a vacuum oven at 80 °C before nanoindentation. According to our previous measurements, this fine polishing procedure is expected to reduce the NMC surface roughness to approximately 4 nm [44].

Preparation of PVDF Binders PVDF powder (HSV900, MTI Co., molecular weight of 600,000) is dissolved in N-Methyl-2-pyrrolidone (NMP) solvent to form a solution containing 6 wt% PVDF. A portion of the mixture is poured into a glass container to prepare for the pure PVDF film, and the remainder of the solution is homogeneously mixed with carbon black (Super P, MTI Co.) in a 50:50 weight ratio in another glass container to prepare for the CB/PVDF film. Both containers are dried in a vacuum oven at 80 °C for a couple of days. The films are easily peeled off from the containers and the final thicknesses are approximately 45 μm for the PVDF film and 400 μm for the CB/PVDF film. Sample weight and dimensions, including volume expansion in the electrolyte, are probed using a micrometer (1μm resolution) and a precision balance (0.1 mg resolution). Measurements are repeated at least three times for each dimension and the average value is used in the estimation of the density and porosity. Sample dimensions and calculation details are provided in Tables S1 and S2. The resulting densities of the PVDF and CB/PVDF films are 1.43 g/cm^3 and 0.80 g/cm^3, respectively. Three CB/PVDF film samples are compressed with an electric rolling press to achieve the final porosities of 50.8%, 27.5%, and 3.8%, respectively. The porosity is estimated based on the difference between measured volume and theoretical volume, as follows:

$$\varepsilon = \frac{V_m - \frac{w_m}{2}\left(\frac{1}{\rho_{\mathrm{PVDF}}} + \frac{1}{\rho_{\mathrm{CB}}}\right)}{V_m}, \tag{1}$$

where V_m is the measured volume of the sample, w_m is the measured weight of the sample, ρ_{PVDF} is 1.45 g/cm^3, and ρ_{CB} is 1.90 g/cm^3.

Mechanical Characterization Nanoindentation (Keysight G200) tests are performed in an argon-filled glovebox (O_2 and $H_2O < 0.5$ ppm). Samples are tested in dry and wet conditions. In wet condition, a stainless-steel coin cell case is used as a container and samples are kept immersed in electrolyte. All samples are allowed to soak in the electrolyte for 1 h before indentation tests. The selected electrolyte, 1 M $LiPF_6$ in propylene carbonate (PC) is nonvolatile, enabling a constant fluid level and salt concentration during tests. In a previous study, we confirmed that the Ar environment and electrolyte solution do not compromise the accuracy of indentation experiments [42].

Hardness H and elastic modulus E are determined using a Berkovich indenter following the Oliver-Pharr method [45]:

$$H = \frac{P}{A}, \tag{2}$$

and

$$\frac{2\beta\sqrt{A_c}}{S\sqrt{\pi}} = \frac{1-\nu^2}{E} + \frac{1-\nu_i^2}{E_i}, \tag{3}$$

where P is the load and β is a geometrical constant (1.034 for Berkovich tip). The elastic modulus and Poisson ratio of the diamond indenter (E_i,ν_i) are 1141 GPa and 0.07, respectively. The continuously measured contact stiffness S is derived from the in-phase material response to a superimposed oscillating signal during dynamic load (also known as continuous stiffness measurement, CSM) [45]. A harmonic displacement of 2 nm and a frequency of 45 Hz are used. The Poisson ratio of the sample, ν, is assumed 0.3 for NMC and 0.4 for PVDF and CB/PVDF, respectively. The area of contact A is derived from the contact indentation depth through an experimentally calibrated function. The indenter is loaded at a constant $\dot{P}/P$ rate of 0.05 s^{-1}, up to the maximum indentation depth (500 nm for NMC and 2000 nm for PVDF and CB/PVDF, respectively). Grid indentations are performed on PVDF and CB/PVDF films with a spacing of 200 μm between each indent. For NMC samples, targeted indentations are conducted at the center of large NMC particles (minimum diameter of 15μm) to minimize the boundary effects.

We measure the fracture toughness K_c of NMC by nanoindentation with a cube-corner indenter. The fracture toughness is calculated following the formula derived by Lawn et al. [46] and Antis et al. [47] for a radial, half-penny crack:

$$K_c = \alpha\left(\frac{E}{H}\right)^{\frac{1}{2}}\frac{P}{c^{3/2}}, \tag{4}$$

where α is an empirical constant that depends on the indenter geometry (0.036 for cube-corner shape [48]), c is the crack length, and P is the critical load that generates a crack of the length c. It is important to note that geometrical variations in the orientation of the indenter relative to the local microstructure (NMC secondary particles) and grain orientation due to crystalline anisotropy (NMC pellet) can be expected to affect the value of the pre-factor α [47]. For instance, anisotropy can introduce a deviation from the ideal half-penny shape crack [49, 50] which may lead to an overestimation of the indentation fracture toughness [51]. However, equation (4) is still useful in the determination of an "effective" toughness, which allows for a quantitative comparison between the NMC materials in the dry and wet states, as the crack pattern is not expected to change from one state to the other. A cube-corner indenter is used because its sharp angle (centerline-to-face angle of 35.3°) reduces the load threshold for cracking [52], enabling the characterization of small volumes of materials such as NMC secondary particles. However, cracks produced at low loads are small and difficult to measure by conventional microscopy techniques. A method proposed by Field et al. [53] allows the estimation of the crack length from the load-displacement curve, which eliminates the need for direct measurement. When a brittle material is indented with a sharp indenter, the load-displacement curve may exhibit sudden bursts in the tip displacement. This sudden tip penetration, so-called pop-in, is thought to be associated with the formation of half-penny cracks extending from the edges of the indenter [53]. The extra tip displacement after the pop-in, h_x, relates to the crack length, c, as follows:

$$c = \sqrt{2}h_m + \left(Q\frac{E'}{H} - \sqrt{2}\right)h_x, \tag{5}$$

where E' is the plane strain elastic modulus, Q is an empirical constant that depends on the indenter geometry (4.55 for cube-corner [53]), h_m is the measured tip displacement, and $h_x = h_m - h_t$. The theoretical tip displacement in the absence of pop-in, h_t, is estimated by the extrapolation of the load-displacement curve before the pop-in event. E' and H are known from indentation tests with the Berkovich tip.

The intricate microstructure of NMC results in a large variation in the load-displacement curves and ambiguity in the detection of pop-in events. Thus, to avoid subjectivity of interpretation and allow efficient handling of numerous experiments, we write an algorithm to process the pop-in data, identify and discard invalid tests, and compute fracture toughness.

The first step of the algorithm is the identification of the pop-in events. Morris et al. [54] showed that pop-in events are associated with peaks in the reduced stiffness, $\overline{S}$,

$$\overline{S} = \frac{S}{S_1}, \tag{6}$$

where S is the continuously measured contact stiffness and S_1 is the instantaneous slope of the loading curve. The inspection of Figure 2(a) shows that, with exception of very small tip displacements, a clear correlation exists between the peaks in $\overline{S}$ (continuous red line) and bursts in the load-displacement behavior (continuous blue line). The algorithm needs to be able to distinguish peaks from random noise in the $\overline{S}$ curve in order to correctly identify pop-in events. Considering the irregularity of the load-displacement curve at very shallow depths, which may also include a pop-in due to elasto-plastic transition [55], a minimum tip displacement h_{min} (black arrow) must be assigned as the threshold below which cracking is assumed not taking place. We choose h_{min}= 100nm. We investigate the sensitivity of the results to this parameter in the Results and Discussion section. Having discarded the reduced stiffness data below h_{min} (continuous grey line), the reduced stiffness data for h above h_{min} (continuous red line) is used to find outliers (pop-ins). Figure 2(b) displays the reduced stiffness distribution for the test in Figure 2(a) where the 'o' symbols represent individual data

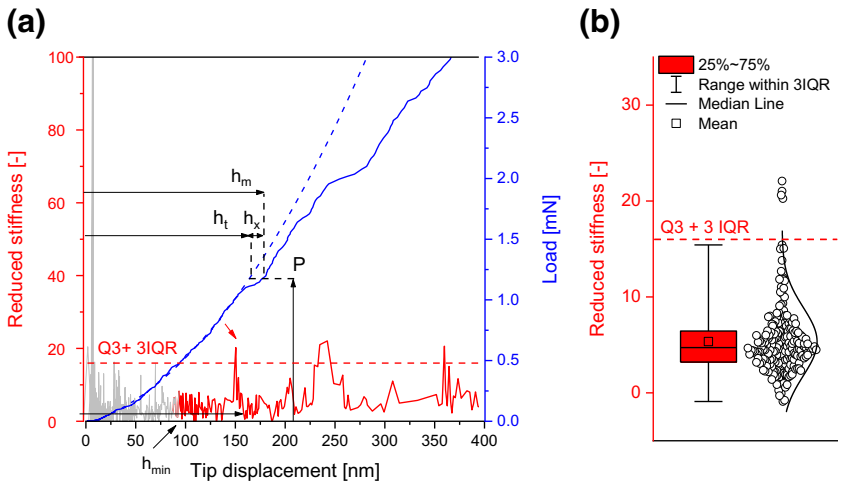

Fig. 2 Systematic procedure for the determination of the fracture toughness. (a) Load as a function of indentation depth and (b) corresponding reduced stiffness distribution showing the $Q3 + 3IQR$ threshold used to characterize a pop-in

points. We define any observations above $Q3 + 3\ IQR$ or below $Q1 - 3\ IQR$ as outliers, where $Q1$ is the 25th percentile and $Q3$ is the 75th percentile, and $IQR = Q3 - Q1$. A real pop-in event will always introduce a positive skewness to the distribution, while random noise leads to a symmetric deviation. Therefore, all pop-in events (outliers) are detected above the upper boundary ($Q3 + 3\ IQR$). The reduced stiffness distribution for each indentation is presented in the supplementary information (Figure S1).

With the pop-in events identified, the load-displacement curve before the first pop-in is fitted with a quadratic polynomial function to predict the theoretical tip displacement without crack h_t (dashed blue line, Figure 2(a)). The crack length is estimated through equation (5) using the pop-in length h_x for the first five points after the pop in event. The validity of equation (5) in the estimation of the crack length for NMC materials was confirmed in our previous work [44]. It is worth noting that the average crack length in our experiments (~1 μm) is much smaller than the radius of the secondary particles (~10 μm), thus avoiding crack interaction with the matrix. Finally, K_c is calculated through equation (4) and the average K_c of the five points is stored. Note that load-displacements curves not are manually selected or removed by the user; only 6% of the total number of tests were automatically discarded by the following criteria: the extrapolated load-displacement curve yields a negative crack length ($h_x < 0$), or no pop-in events are detected.

Results and Discussion

We measure the individual mechanical properties of PVDF polymeric binder, CB/PVDF conductive matrix, and NMC particles in the 1 M $LiPF_6$-PC liquid electrolyte. NMC532 is investigated in the form of secondary particles (small grains) and sintered pellet (large grains). The conductive matrix is examined for different porosities and with and without carbon black filler.

Modulus and Hardness of the Binder and the Conductive Matrix

Electrolyte uptake causes a volume strain of roughly 30% in the PVDF film (Figure 3(a)). This large volumetric change alters the functionality of the conductive matrix in different aspects. For instance, the increase in the binder volume represents an effective decrease in the volume ratio of the conductive filler (i.e., carbon black), and consequently causes an increase in the electrical resistance of the electrode [56, 57]. For the CB/PVDF composite, the volume expansion depends on the initial porosity. We find that the dense film expands 30% in volume as compared to 15% volume expansion for the porous film (50% porosity). Thus, the increase in the specific volume of the binder in wet condition would occupy pore spaces in the conductive matrix, which could affect the ion transport. It is interesting to note that volume expansion

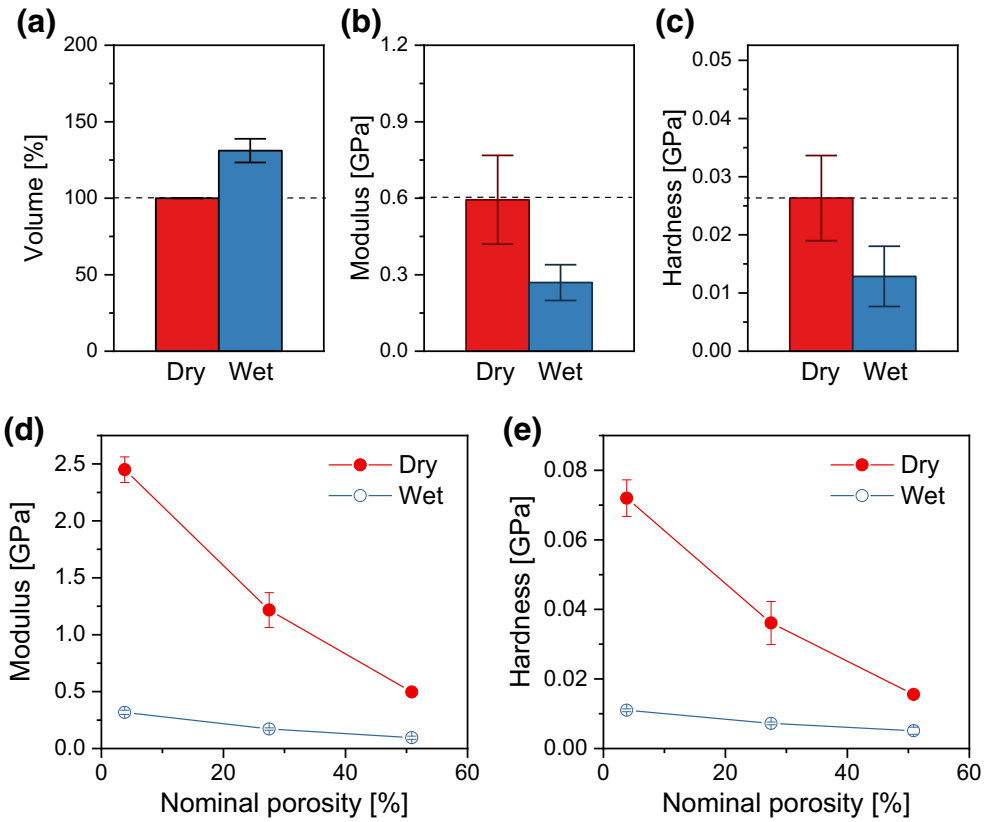

Fig. 3 The comparisons of (a) volume, (b) elastic modulus, and (c) hardness of the PVDF binder under dry and wet conditions. (d) Elastic modulus and (e) hardness of the CB/PVDF conductive matrix as a function of the nominal porosity. Dry measurements are shown in red and wet measurements are shown in blue. The error bars represent the standard deviation

displays an opposite trend to the swelling ratio (weight fraction increase by electrolyte uptake) as reported in literature which increases with the porosity [58]. The thicknesses of pure PVDF and CB/PVDF films (50 and 185–420 μm, respectively) are sufficiently large so that the elastic modulus and hardness are approximately constant with different indentation depths (no substrate effect), Figures S2 and S3. The elastic modulus of PVDF film in dry condition, 590 MPa (red bar, Figure 3(b)), is in good agreement with previous reports by tensile tests (400–650 MPa) [56, 59]. In the wet condition, both the elastic modulus and the hardness of the binder drop by about 50% (blue bar, Figure 3(b) and (c)). This deterioration in the mechanical properties is a result of binder expansion by solvent uptake which facilitates sliding and disentanglement of the polymer chains [60].

The CB filler has a significant impact on the mechanical behavior of the dry matrix - the modulus of the CB/PVDF composite (2.5–2 GPa, Figure 3(d)) is about four times that of pure PVDF (0.59 GPa, Figure 3(b)). Both modulus and hardness decrease significantly with the porosity, Figures 3(d) and (e), where the nominal porosity represents the initial porosity of the matrix without absorption of liquid. The effect of electrolyte soaking is particularly detrimental to the properties of the conductive matrix (CB/PVDF), resulting in a decrease of over 80% in both modulus and hardness. In the wet state, the mechanical properties of PVDF and CB/PVDF are roughly the same, indicating that the carbon black loses most of its role in the mechanical response of the composite.

Modulus, Hardness, and Fracture Strength of NMC Secondary Particles and Pellets

The NMC material is evaluated in two configurations: as-received hierarchical particles (small grains) and sintered pellet (large grains). The final grain size of the pellet (3–10 μm, Figure 4(a)) is significantly larger than the size of the primary particles in the as-received NMC sample (0.1–1 μm, Figure 4(b)). The XRD profile of the NMC pellet is consistent with the reference pattern [61], confirming that the elemental composition and crystal structure are maintained during sintering (Figure 4(c)). For the hierarchical particles, a PS matrix is used to hold the particles during indentation. Figure 5 confirms that the elastic modulus (3.8 GPa) and the hardness (0.25 GPa) of the PS matrix remain unchanged in the presence of the electrolyte, thus attributing the changes in the measured mechanical behavior in dry versus wet environments to the NMC particles alone. Targeted indentations are performed on the polished NMC samples. The surface finish, microstructure and indentation sites are shown in Figure 6(a) (NMC secondary particles embedded in PS matrix) and in Figure 6(b) (sintered NMC pellet). The low resolution of Figure 6(a) is partly because of the poor electrical conductivity of the PS matrix. While both samples exhibit a certain degree of porosity, the primary particle size differs significantly. At an appropriate indentation depth, this difference allows probing the mechanical response within a single particle (sintered NMC pellet) and across particle interfaces (as-received

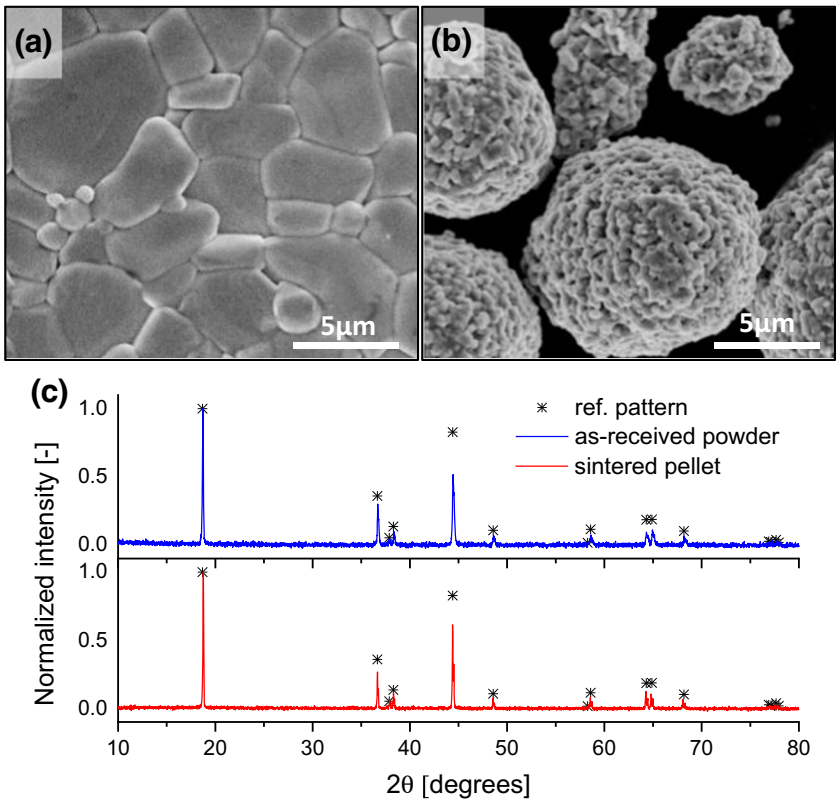

Fig. 4 SEM image of the NMC532 (a) sintered pellet and (b) as-received secondary particles. (c) XRD profiles in comparison with the reference pattern [58]

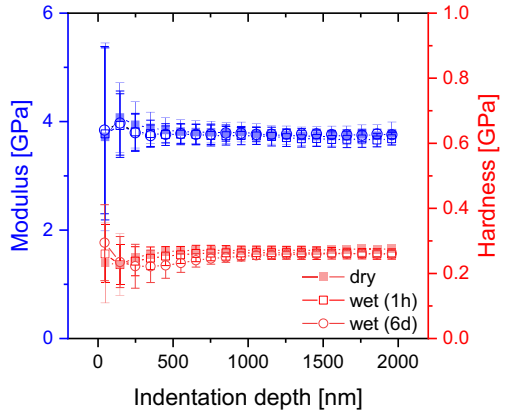

Fig. 5 Elastic modulus (blue) and hardness (red) of polystyrene in dry condition (filled square), submerged in 1 M $LiPF_6$-PC electrolyte for 1 h (open square), and submerged in the electrolyte for 6 days (open circle). The error bars represent the standard deviation

NMC powder). The pellet experiment is approximate to the intrinsic properties of NMC in the bulk form, while the measurement of NMC secondary particles is dependent on the packing arrangement of the agglomerate, porosity, and physical interactions between the primary particles.

For elastic modulus and hardness measurements, a minimum of 15 indentations are performed for each configuration. The load-displacement curve and elastic modulus as a function of indentation depth are shown in Figure 7. The decrease in modulus with indentation depth is a consequence of two main reasons: (i) the substrate effect, and (ii) deep indentation induced material damage. In an earlier work, we showed that tests on NMC particles are independent on the matrix properties if the indentation site is away from the particle/matrix interface and if the indentation depth is chosen much less than the secondary particle radius (8–10 μm) [44]. Potential crack formation and propagation in a brittle material induced by deep indentation is another reason of the decrease of modulus [62, 63]. The dashed line in Figure 7(b) indicates the selected indentation depth (85 nm) to minimize material damage. This value represents the lowest indentation depth where the surface roughness is negligible while the area function calibration and surface contact detection remains accurate in our experiments.

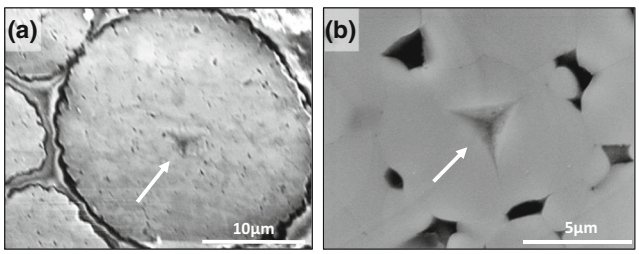

Fig. 6 SEM images of the polished NMC agglomerates in a polystyrene matrix (a) and sintered pellet (b). The residual impressions at the preselected sites are shown after removal of the indenter

Figure 8 shows the elastic modulus, hardness and fracture toughness of NMC sintered pellet and secondary particles (NMC agglomerates) in dry (red box) and wet (blue box) conditions. The grey circles represent individual indentations, the box indicates the 25–75% range, the white line is the median, and the average values are shown in the labels and indicated by the white squares. Regardless of the environment effect, the mechanical properties of the agglomerated secondary particles are generally lower than those of sintered pellets. This difference is attributed to the weak interfaces between the primary particles in the NMC agglomerate. Kendall et al. [64] showed that the contact between particles within an agglomerate introduces compliance to the system and results in a lower elastic modulus of the assembly. The modulus of the agglomerate is dependent on the packing ratio, the diameter of the primary particles, and the interfacial energy [64]. Thus, the synthesis procedure of NMC powder, which strongly affects the particle morphology and internal porosity [65, 66], can have significant impact on the mechanical properties of the agglomerate.

There is no apparent difference between the elastic modulus and hardness of NMC samples in dry versus wet condition. However, while the properties of sintered pellets remain mostly unchanged in the electrolyte, the average fracture toughness of the secondary particles is improved from 0.104 MPa $m^{\frac{1}{2}}$ in the dry condition to 0.212 MPa $m^{\frac{1}{2}}$ in the liquid environment. This difference is statistically significant according to the standard t-test (p value = 0.007). It is worth noting that for the computation of the fracture toughness, we assumed that the threshold for cracking was h_{min} = 100 nm. To test the sensitivity of the calculations to this parameter we compute K_c for h_{min} = 50 nm and h_{min} = 150 nm, Figure S4. The trend is the same, however, h_{min} = 100 nm results in the least number of discarded tests and at the same time, the least spread in the data. The detailed fracture toughness calculation for each individual test is provided in the supplementary information, Figures S5-S8. These results suggest that crack propagating along the interface of primary particles is influenced by the liquid penetration. Notice that, for the secondary particles, the variation in the data is significantly higher in wet condition than in dry state. This variation is not observed for the pellet measurements. The large deviation is likely a result of heterogeneity in liquid saturation rather than random noise in the experiments. To better understand the behavior, we first consider the nature of the bonding forces in granules.

For granular materials, the strength of an agglomerate is governed by interparticle bonding rather than the strength of the individual constituent particles [67]. Rumpf and Schubert [68] considered the adhesion between single particles including the following mechanisms: (i) bonds without material bridges (van der Waals, electrostatic, and magnetic forces), and (ii) bonds with material bridges that can be liquid or solid

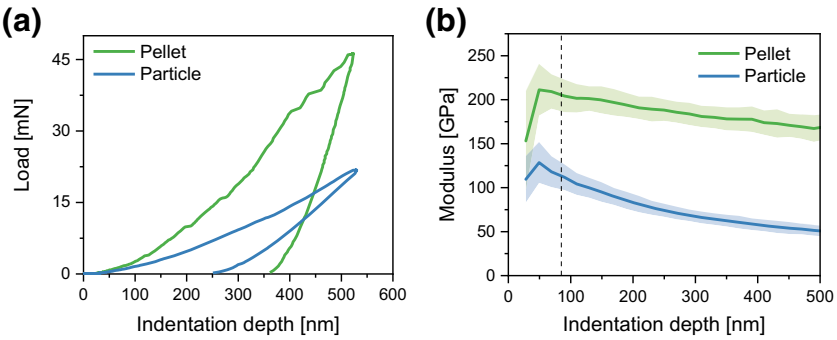

Fig. 7 (a) Load-displacement curves and (b) elastic modulus as a function of the indentation depth for NMC particles and pellet. The shaded areas in (b) represent the standard deviation

(binding agents, sintering, crystallizing salts). The relative importance of the bonding forces varies case by case. NMC powder is usually synthesized via the two-step process: (i) precursors are fabricated by hydroxide co-precipitation; and (ii) precursors are mixed in appropriate proportions and calcinated [66, 69]. The resulting powder consists of secondary particles in which many primary particles are aggregated, Figure 9(a). The characteristic sizes of primary particles, in the range of several hundred nanometers, are sufficiently small such that van der Waals forces can be significant. It is also possible that chemical bonds form along particle boundaries depending on the calcination conditions.

Because of the high polydispersity and irregular particle shapes, it is impractical to obtain precise analytical predictions for the strength of the NMC agglomerates. As a first approximation, we use the classical Rumpf model to represent the tensile strength σ_t of agglomerates composed of spherical particles of a uniform size:

$$\sigma_t = nF = 1.1\left(\frac{1-\varepsilon}{\varepsilon}\right)\left(\frac{1}{D^2}\right)F, \tag{7}$$

where n is the average number of interparticle contacts per unit area of the cross-section and F is binding force. This equation is applicable for different bonding mechanisms. Our initial speculation was that the liquid electrolyte may act as a lubricant in the NMC agglomerate which reduces the inter-particle friction and thus the interlocking forces in the secondary particles. However, the experimental result suggests otherwise. Compared to the dry state, the wetted agglomerate possesses negative capillary pressure which absorbs liquid electrolyte into the microchannels between primary particles, Figure 9(b). Capillary forces are typically stronger than van der Waals attraction but weaker than the solid bridges, and therefore can potentially impact the strength of NMC agglomerates. To evaluate the magnitude of the additional capillary force brought by the liquid bridging, we rewrite equation (7) using capillary forces F [68]:

$$\sigma_t = 6S\frac{1-\varepsilon}{\varepsilon}\frac{\gamma}{D}cos\theta, \tag{8}$$

where S is the liquid saturation, ε is the void fraction, D is the surface average diameter of primary particles, γ is the surface tension, and θ is the liquid-solid contact angle. The surface tension of the PC solution is 41.1 mN/m [70]. Assuming $\theta = 0$, a saturation value of 0.95, and void fraction of 0.028 [71], equation (8) predicts a fracture strength of ~16 MPa for NMC primary particles bonded only by the capillary forces. We calculate the interfacial strength using linear elastic fracture mechanics: $K_{IC} = \sigma_t\sqrt{\pi a}/Y$. Assuming a half crack length a of $1\mu m$ and a half penny surface crack ($Y = 0.64$),

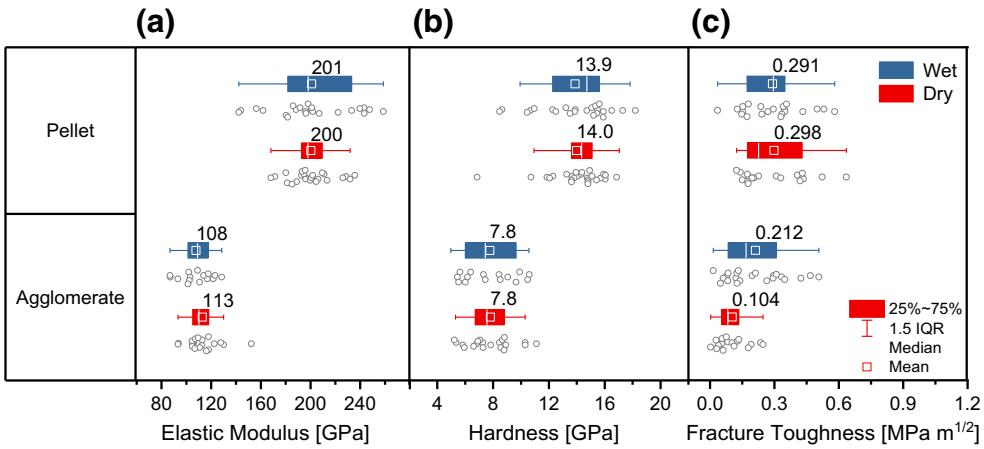

Fig. 8 (a) Elastic modulus, (b) hardness, and (c) fracture toughness of NMC agglomerate and sintered pellet in dry (red box) and wet (blue box) environment

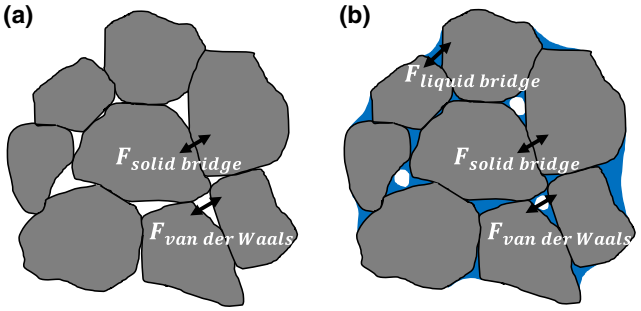

Fig. 9 Schematic illustration of physical interactions between the primary particles in dry (a) and wet (b) conditions

we find an increase of 0.044 MPa $m^{1/2}$ in fracture toughness of NMC secondary particles in the liquid electrolyte compared to its dry state. This difference is on the similar order of magnitude as determined in experiments (median difference of 0.085 MPa $m^{1/2}$ and average difference of 0.108 MPa $m^{1/2}$). It is worth noting that the analysis is based on an idealized model of spherical primary particles of a uniform size, while the as-synthesized NMC particles are polydisperse and of irregular shapes. In addition, previous work has shown that the Rumpf model may largely underestimate the strength of granular materials [64]. Here we use the theoretical calculations to evaluate the liquid bridging due to the capillary forces which can be significant in determining the interfacial strength of the agglomerated particles. Other mechanisms are also possible underpinning the liquid effect. For example, previous work showed that the native oxide SiO_x on Si anodes can react with the decomposition products of $LiPF_6$ (PF_5 or HF in trace amounts in the electrolyte) to form SiO_yF_z at the ambient temperate prior to electrochemical cycles [29]. A solid surface layer may act as a nano-filler at the interface of primary particles and alter the interfacial strength of the secondary particles. Further experiments are necessary to fully understand the bonding nature of NMC agglomerates in the liquid environment.

Conclusions

We use in-situ nanoindentation in an inert environment to measure the mechanical properties of a PVDF polymeric binder, a CB/PVDF conductive matrix, and NMC active materials in dry and wet conditions. Commercial NMC cathode is studied in the form of as-received secondary particles (agglomerate of primary particles) and sintered pellet (large single particles). For both configurations, there is no apparent difference between the elastic modulus and hardness in dry and wet states. The fracture toughness of sintered pellets remains mostly unchanged in both conditions, while the interfacial strength of the secondary particles is largely enhanced when submersed in the electrolyte. The result suggests that crack in an NMC agglomerate propagates along the interfaces between primary particles and is influenced by the liquid saturation. A possible reason is the capillary pressure that absorbs liquid electrolyte into the microchannels and nanopores between primary particles, creating an additional bonding force. The mechanical response of conductive matrix is largely dependent on the porosity and carbon content in dry condition. When wetted by electrolyte, the PVDF binder undergoes a volume expansion of up to 30% and a decrease in the elastic modulus and hardness of roughly 50%. The effect of electrolyte soaking is particularly detrimental to the mechanical strength of the conductive matrix (CB/PVDF), which results in a decrease of over 80% in the mechanical properties. Experimental results highlight the significance of the liquid environment on the mechanical behavior of both active materials and conductive agents in composite electrodes.

Acknowledgements We are grateful for the support by the National Science Foundation through the grants DMR-1832707 and CMMI-1726392.

References

1. Whittingham MS (2008) Materials challenges facing electrical energy storage. MRS Bull 33:411–419. https://doi.org/10.1557/mrs2008.82
2. Xu R, Zhao K (2016) Electrochemomechanics of Electrodes in Li-Ion Batteries: A Review. J Electrochem Energy Convers Storage 13:030803. https://doi.org/10.1115/1.4035310
3. Kusoglu A, Weber AZ (2015) Electrochemical/Mechanical Coupling in Ion-Conducting Soft Matter. J Phys Chem Lett 6:4547–4552. https://doi.org/10.1021/acs.jpclett.5b01639
4. Wang H, Jang Y, Huang B et al (1999) TEM Study of Electrochemical Cycling-Induced Damage and Disorder in $LiCoO_2$ Cathodes for Rechargeable Lithium Batteries. J Electrochem Soc 146:473–480. https://doi.org/10.1149/1.1391631
5. Gabrisch H, Yazami R, Fultz B (2002) The Character of Dislocations in $LiCoO_2$. Electrochem Solid-State Lett 5:A111–A114. https://doi.org/10.1149/1.1472257
6. Kim NY, Yim T, Song JH et al (2016) Microstructural study on degradation mechanism of layered $LiNi_{0.6}Co_{0.2}Mn_{0.2}O_2$ cathode materials by analytical transmission electron microscopy. J Power Sources 307:641–648. https://doi.org/10.1016/j.jpowsour.2016.01.023
7. Ning G, Haran B, Popov BN (2003) Capacity fade study of lithium-ion batteries cycled at high discharge rates. J Power Sources 117:160–169. https://doi.org/10.1016/S0378-7753(03)00029-6
8. Miller DJ, Proff C, Wen JG et al (2013) Observation of microstructural evolution in li battery cathode oxide particles by in situ electron microscopy. Adv Energy Mater 3:1098–1103. https://doi.org/10.1002/aenm.201300015
9. Wang D, Wu X, Wang Z, Chen L (2005) Cracking causing cyclic instability of $LiFePO_4$ cathode material. J Power Sources 140:125–128. https://doi.org/10.1016/J.jpowsour.2004.06.059
10. Zhao K, Pharr M, Hartle L et al (2012) Fracture and debonding in lithium-ion batteries with electrodes of hollow core-shell nanostructures. J Power Sources 218:6–14. https://doi.org/10.1016/j.jpowsour.2012.06.074
11. Zhao K, Pharr M, Vlassak JJ, Suo Z (2010) Fracture of electrodes in lithium-ion batteries caused by fast charging. J Appl Phys 108:073517. https://doi.org/10.1063/1.3492617

12. Jaguemont J, Boulon L, Dubé Y (2016) A comprehensive review of lithium-ion batteries used in hybrid and electric vehicles at cold temperatures. Appl Energy 164:99–114. https://doi.org/10.1016/j.apenergy.2015.11.034
13. Deshpande R, Verbrugge M, Cheng Y-T et al (2012) Battery Cycle Life Prediction with Coupled Chemical Degradation and Fatigue Mechanics. J Electrochem Soc 159:A1730–A1738. https://doi.org/10.1149/2.049210jes
14. Pharr M, Suo Z, Vlassak JJ (2013) Measurements of the fracture energy of lithiated silicon electrodes of Li-Ion batteries. Nano Lett 13:5570–5577. https://doi.org/10.1021/nl403197m
15. Ebner M, Marone F, Stampanoni M, Wood V (2013) Visualization and Quantification of Electrochemical and Mechanical Degradation in Li Ion Batteries. Science (80-) 342:716–721. https://doi.org/10.1126/science.1241882
16. Cabana J, Monconduit L, Larcher D, Palacín MR (2010) Beyond intercalation-based Li-ion batteries: The state of the art and challenges of electrode materials reacting through conversion reactions. Adv Mater 22:170–192. https://doi.org/10.1002/adma.201000717
17. Liu XH, Liu Y, Kushima A et al (2012) In situ TEM experiments of electrochemical lithiation and delithiation of individual nanostructures. Adv Energy Mater 2:722–741. https://doi.org/10.1002/aenm.201200024
18. Beaulieu LY, Eberman KW, Turner RL et al (2001) Colossal Reversible Volume Changes in Lithium Alloys. Electrochem Solid-State Lett 4:A137–A140. https://doi.org/10.1149/1.1388178
19. Yan P, Zheng J, Gu M et al (2017) Intragranular cracking as a critical barrier for high-voltage usage of layer-structured cathode for lithium-ion batteries. Nat Commun 8:1–9. https://doi.org/10.1038/ncomms14101
20. Mu L, Lin R, Xu R et al (2018) Oxygen Release Induced Chemomechanical Breakdown of Layered Cathode Materials. Nano Lett 18:3241–3249. https://doi.org/10.1021/acs.nanolett.8b01036
21. Sun G, Sui T, Song B et al (2016) On the fragmentation of active material secondary particles in lithium ion battery cathodes induced by charge cycling. Extrem Mech Lett 9:449–458. https://doi.org/10.1016/j.eml.2016.03.018
22. Song B, Sui T, Ying S et al (2015) Nano-structural changes in Li-ion battery cathodes during cycling revealed by FIB-SEM serial sectioning tomography. J Mater Chem A 3:18171–18179. https://doi.org/10.1039/C5TA04151A
23. Li G, Zhang Z, Huang Z et al (2017) Understanding the accumulated cycle capacity fade caused by the secondary particle fracture of $LiNi_{1-x-y}Co_xMn_yO_2$ cathode for lithium ion batteries. J Solid State Electrochem 21:673–682. https://doi.org/10.1007/s10008-016-3399-9
24. Xu R, de Vasconcelos LS, Shi J et al (2018) Disintegration of Meatball Electrodes for $LiNi_xMn_yCo_zO_2$ Cathode Materials. Exp Mech 58:549–559. https://doi.org/10.1007/s11340-017-0292-0
25. Cao PF, Naguib M, Du Z et al (2018) Effect of Binder Architecture on the Performance of Silicon/Graphite Composite Anodes for Lithium Ion Batteries. ACS Appl Mater Interfaces 10:3470–3478. https://doi.org/10.1021/acsami.7b13205
26. Choi S, woo KT, Coskun A, Choi JW (2017) Highly elastic binders integrating polyrotaxanes for silicon microparticle anodes in lithium ion batteries. Science (80-) 357:279–283. https://doi.org/10.1126/science.aal4373
27. Xu R, Scalco De Vasconcelos L, Zhao K (2016) Computational analysis of chemomechanical behaviors of composite electrodes in Li-ion batteries. J Mater Res 31:2715–2727. https://doi.org/10.1557/jmr.2016.302
28. McDowell MT, Ryu I, Lee SW et al (2012) Studying the kinetics of crystalline silicon nanoparticle lithiation with in situ transmission electron microscopy. Adv Mater 24:6034–6041. https://doi.org/10.1002/adma.201202744
29. Nguyen CC, Yoon T, Seo DM et al (2016) Systematic Investigation of Binders for Silicon Anodes: Interactions of Binder with Silicon Particles and Electrolytes and Effects of Binders on Solid Electrolyte Interphase Formation. ACS Appl Mater Interfaces 8:12211–12220. https://doi.org/10.1021/acsami.6b03357
30. Iqbal N, Lee S (2018) Mechanical Failure Analysis of Graphite Anode Particles with PVDF Binders in Li-Ion Batteries. J Electrochem Soc 165:A1961–A1970. https://doi.org/10.1149/2.0111810jes
31. Amanieu H-Y, Rosato D, Sebastiani M et al (2014) Mechanical property measurements of heterogeneous materials by selective nanoindentation: Application to $LiMn_2O_4$ cathode. Mater Sci Eng A 593:92–102. https://doi.org/10.1016/j.msea.2013.11.044
32. de Vasconcelos LS, Xu R, Li J, Zhao K (2016) Grid indentation analysis of mechanical properties of composite electrodes in Li-ion batteries. Extrem Mech Lett 9:495–502. https://doi.org/10.1016/j.eml.2016.03.002
33. Qu M, Woodford WH, Maloney JM et al (2012) Nanomechanical Quantification of Elastic, Plastic, and Fracture Properties of $LiCoO_2$. Adv Energy Mater 2:940–944. https://doi.org/10.1002/aenm.201200107
34. Swallow JG, Woodford WH, McGrogan FP et al (2014) Effect of Electrochemical Charging on Elastoplastic Properties and Fracture Toughness of Li_XCoO_2. J Electrochem Soc 161:F3084–F3090. https://doi.org/10.1149/2.0141411jes
35. Kim D, Shim HC, Yun TG et al (2016) High throughput combinatorial analysis of mechanical and electrochemical properties of $Li[Ni_xCo_yMn_z]O_2$ cathode. Extrem Mech Lett 9:439–448. https://doi.org/10.1016/j.eml.2016.03.019
36. Berla LA, Lee SW, Cui Y, Nix WD (2015) Mechanical behavior of electrochemically lithiated silicon. J Power Sources 273:41–51. https://doi.org/10.1016/j.jpowsour.2014.09.073
37. Mughal MZ, Moscatelli R, Amanieu HY, Sebastiani M (2016) Effect of lithiation on micro-scale fracture toughness of $Li_xMn_2O_4$ cathode. Scr Mater 116:62–66. https://doi.org/10.1016/j.scriptamat.2016.01.023
38. Amanieu H-Y, Aramfard M, Rosato D et al (2015) Mechanical properties of commercial $LixMn_2O_4$ cathode under different States of Charge. Acta Mater 89:153–162. https://doi.org/10.1016/j.actamat.2015.01.074
39. Wohlfahrt-Mehrens M, Vogler C, Garche J (2004) Aging mechanisms of lithium cathode materials. J Power Sources 127:58–64. https://doi.org/10.1016/j.jpowsour.2003.09.034
40. Wang Y, Zhang Q, Li D et al (2018) Mechanical property evolution of silicon composite electrodes studied by environmental nanoindentation. Adv Energy Mater 8:1–8. https://doi.org/10.1002/aenm.201702578
41. Wendt C, Niehoff P, Winter M, Schappacher FM (2018) Determination of the mechanical integrity of polyvinylidene difluoride in $LiNi_{1/3}Co_{1/3}Mn_{1/3}O_2$ electrodes for lithium ion batteries by use of the micro-indentation technique. J Power Sources 391:80–85. https://doi.org/10.1016/j.jpowsour.2018.03.064
42. de Vasconcelos LS, Xu R, Zhao K (2017) Operando nanoindentation: a new platform to measure the mechanical properties of electrodes during electrochemical reactions. J Electrochem Soc 164:A3840–A3847. https://doi.org/10.1149/2.1411714jes
43. Magasinski A, Zdyrko B, Kovalenko I et al (2010) Toward efficient binders for Li-ion battery Si-based anodes: Polyacrylic acid. ACS Appl Mater Interfaces 2:3004–3010. https://doi.org/10.1021/am100871y
44. Xu R, Sun H, de Vasconcelos LS, Zhao K (2017) Mechanical and Structural Degradation of $LiNi_xMn_yCo_zO_2$ Cathode in Li-Ion Batteries: An Experimental Study. J Electrochem Soc 164:A3333–A3341. https://doi.org/10.1149/2.1751713jes

45. Oliver WC, Pharr GM (1992) An improved technique for determining hardness and elastic modulus using load and displacement sensing indentation experiments. J Mater Res 7:1564–1583
46. Marshall DB, Lawn BR, Evans AG (1982) Elastic/plastic indentation damage in ceramics: the lateral crack system. J Am Ceram Soc 65:561–566. https://doi.org/10.1111/j.1151-2916.1982.tb10782.x
47. Chantikul P, Anstis GR, Lawn BR, Marshall DB (1981) A critical evaluation of indentation techniques for measuring fracture toughness: II, strength method. J Am Ceram Soc 64:539–543. https://doi.org/10.1111/j.1151-2916.1981.tb10321.x
48. Harding DS, Oliver WC, Pharr GM (1994) Cracking During Nanoindentation and its Use in the Measurement of Fracture Toughness. MRS Proc 356:663–668. https://doi.org/10.1557/proc-356-663
49. Anstis GR, Chantikul P, Lawn BR, Marshall DB (1981) A Critical Evaluation of Indentation Techniques for Measuring Fracture Toughness I. Direct Crack Measurements 46:533–538
50. Diercks DR, Musselman M, Morgenstern A et al (2014) Evidence for Anisotropic Mechanical Behavior and Nanoscale Chemical Heterogeneity in Cycled $LiCoO_2$. J Electrochem Soc 161:F3039–F3045. https://doi.org/10.1149/2.0071411jes
51. Calderon-Moreno J, Popa M (2001) Fracture toughness anisotropy by indentation and SEVNB on tetragonal PZT polycrystals. Mater Sci Eng A 319–321:692–696. https://doi.org/10.1016/S0921-5093(00)02020-7
52. il JJ, Pharr GM (2008) Influence of indenter angle on cracking in Si and Ge during nanoindentation. Acta Mater 56:4458–4469. https://doi.org/10.1016/j.actamat.2008.05.005
53. Field JS, Swain MV, Dukino JD (2003) Determination of fracture toughness from the extra penetration produced by indentation pop-in. J Mater Res 18:1412–1416. https://doi.org/10.1557/jmr.2003.0194
54. Morris DJ, Myers SB, Cook RF (2004) Sharp probes of varying acuity: Instrumented indentation and fracture behavior. J Mater Res 19:165–175. https://doi.org/10.1557/jmr.2004.0020
55. Scholz T, Schneider GA, Muñoz-Saldaña J, Swain MV (2004) Fracture toughness from submicron derived indentation cracks. Appl Phys Lett 84:3055–3057. https://doi.org/10.1063/1.1711164
56. Chen Z, Christensen L, Dahn JR (2003) Comparison of PVDF and PVDF-TFE-P as Binders for Electrode Materials Showing Large Volume Changes in Lithium-Ion Batteries. J Electrochem Soc 150:A1073–A1078. https://doi.org/10.1149/1.1586922
57. Komaba S, Shimomura K, Yabuuchi N et al (2011) Study on polymer binders for high-capacity SiO negative electrode of Li-Ion batteries. J Phys Chem C 115:13487–13495. https://doi.org/10.1021/jp201691g
58. Chung NK, Kwon YD, Kim D (2003) Thermal, mechanical, swelling, and electrochemical properties of poly(vinylidene fluoride)-co-hexafluoropropylene/poly(ethylene glycol) hybrid-type polymer electrolytes. J Power Sources 124:148–154. https://doi.org/10.1016/S0378-7753(03)00608-6
59. Liu ZH, Maréchal P, Jérôme R (1998) Blends of poly(vinylidene fluoride) with polyamide 6: interfacial adhesion, morphology and mechanical properties. Polymer (Guildf) 39:1779–1785. https://doi.org/10.1016/S0032-3861(97)00222-X
60. Chen Z, Christensen L, Dahn JR (2004) Mechanical and Electrical Properties of Poly(vinylidene fluoride–tetrafluoroethylene–propylene)/Super-S Carbon Black Swelled in Liquid Solvent as an Electrode Binder for Lithium-Ion Batteries. J Appl Polym Sci 91:2958–2965
61. Gu Y-J, Zhang Q-G, Chen Y-B et al (2015) Reduction of the lithium and nickel site substitution in $Li_{1+x}Ni_{0.5}Co_{0.2}Mn_{0.3}O_2$ with Li excess as a cathode electrode material for Li-ion batteries. J Alloys Compd 630:316–322. https://doi.org/10.1016/j.jallcom.2014.12.235
62. Quinn JB, Quinn GD (1997) Indentation brittleness of ceramics: a fresh approach. J Mater Sci 32:4331–4346. https://doi.org/10.1023/A:1018671823059
63. Ebisu T, Horibe S (2010) Analysis of the indentation size effect in brittle materials from nanoindentation load–displacement curve. J Eur Ceram Soc 30:2419–2426. https://doi.org/10.1016/j.jeurceramsoc.2010.05.006
64. Kendall K, McN Alford N, Birchall JD et al (1987) Elasticity of Particle Assemblies as a Measure of the Surface Energy of Solids. Source Proc R Soc London Ser A, Math Phys Sci 412:269–283. https://doi.org/10.2307/2398151
65. Lee MH, Kang YJ, Myung ST, Sun YK (2004) Synthetic optimization of $Li[Ni_{1/3}Co_{1/3}Mn_{1/3}]O_2$ via co-precipitation. Electrochim Acta 50:939–948. https://doi.org/10.1016/j.electacta.2004.07.038
66. Wu K, Wang F, Gao L et al (2012) Effect of precursor and synthesis temperature on the structural and electrochemical properties of $Li(Ni_{0.5}Co_{0.2}Mn_{0.3})O_2$. Electrochim Acta 75:393–398. https://doi.org/10.1016/j.electacta.2012.05.035
67. Reynolds GK, Fu JS, Cheong YS et al (2005) Breakage in granulation: A review. Chem Eng Sci 60:3969–3992. https://doi.org/10.1016/j.ces.2005.02.029
68. Rumpf H, Schubert H (1974) The behavior of agglomerates under tensile strain. J Chem Eng Japan 7:294–298. https://doi.org/10.1252/jcej.7.294
69. Jouanneau S, Eberman KW, Krause LJ, Dahn JR (2003) Synthesis, Characterization, and Electrochemical Behavior of Improved $Li[Ni_xCo_{1-2x}Mn_x]O_2$ ($0.1 \le x \le 0.5$). J Electrochem Soc 150:A1637–A1642. https://doi.org/10.1149/1.1622956
70. Sheng Y (2015) Investigation of electrolyte wetting in lithium ion batteries: effects of electrode pore structures and solution. Dissertation, The University of Wisconsin-Milwaukee
71. Watanabe S, Kinoshita M, Hosokawa T et al (2014) Capacity fading of $LiAl_yNi_{1-x-y}Co_xO_2$ cathode for lithium-ion batteries during accelerated calendar and cycle life tests (effect of depth of discharge in charge-discharge cycling on the suppression of the micro-c). J Power Sources 260:50–56. https://doi.org/10.1016/j.jpowsour.2014.02.103